



## **Final Draft** **of the original manuscript**

Froend, M.; Ventzke, V.; Kashaev, N.; Klusemann, B.; Enz, J.:

**Thermal analysis of wire-based direct energy deposition of Al-Mg using different laser irradiances.**

In: Additive Manufacturing. Vol. 29 (2019) 100800.

First published online by Elsevier: 29.07.2019

<https://dx.doi.org/10.1016/j.addma.2019.100800>

# Thermal analysis of wire-based direct energy deposition of Al-Mg using different laser irradiances

M. Froend<sup>a,\*</sup>, V. Ventzke<sup>a</sup>, N. Kashaev<sup>a</sup>, B. Klusemann<sup>a,b</sup>, J. Enz<sup>a</sup>

<sup>a</sup>*Helmholtz-Zentrum Geesthacht, Institute of Materials Research, Materials Mechanics, Max-Planck-Straße 1, D-21052 Geesthacht, Germany*

<sup>b</sup>*Leuphana University of Lüneburg, Institute of Product and Process Innovation, Universitätsallee 1, D-21335 Lüneburg, Germany*

---

## Abstract

The wire-based deposition of metallic light-weight materials such as titanium or aluminium alloys has recently received increasing attention in industry and academia. In particular, the focus is on the processing of high deposition rates, which strongly contributes to good economic production. However, this is mostly associated with process-limiting phenomena such as the development of high temperatures resulting in poor surface finish as well as coarse and unidirectional solidification microstructures. In this regard, laser systems, which are already widely used in industrial processes, allow for a great variety in the controllability of energy inputs, thereby enabling the control of process temperatures and resulting microstructures. The subject of the current study is the detailed elucidation and evaluation of important features such as the development of temperature gradients, resulting cooling rates and thermal cycles for different laser irradiation intensities in order to gain insights for further improvements of the process. Significant heat accumulation and process instabilities at high irradiation intensities and inhomogeneous thermal profiles along the length and height of the parts were observed. In contrast, lower irradiation intensities resulted in a more stable process with increased cooling rates, which

---

\*Corresponding author

*Email address:* martin.froend@hzg.de (M. Froend)

favourably influenced the reduction in thermal stresses as well as refinement of the solidification structure.

*Keywords:* Laser Additive Manufacturing; Aluminium alloy; Infrared Thermography; Laser Metal Deposition; Thermal analysis

---

## 1. Introduction

Laser metal deposition (LMD) is a melt solidification process that uses laser energy to melt the processed material [1, 2, 3, 4]. It has similarities to fusion welding processes such as laser beam welding (LBW) enhanced by the layered addition of a specific material, which is the key method in additive manufacturing [2, 3, 4, 5]. Already gained knowledge in the field of LBW can therefore be transferred to wire-based LMD processes. Recent publications have demonstrated the feasibility of wire-based LMD of Al-Mg alloys [3, 6]. The high degree of reflection, as well as the strong tendency of pore development in the processing  
10 of Al represent great challenges regarding the achievement of sufficient melting and homogeneous solidification. By this, the amount of heat input as well as its feasibility during wire-based LMD of Al is an important aspect.

As already investigated by Leong and Geyer [7, 8], laser irradiance is one main parameter to describe the required energy input to melt a material in laser-assisted fusion processes. Therefore, the transfer from LBW to AM processes as well as the detailed characterization of its influence is assumed to give relevant information with respect to process controllability. Due to the fact that the developed temperatures in fusion-based processes of metals have great effects on important characteristics such as microstructure, residual stresses or stability of  
20 the chemical composition, their investigation is urgently needed to understand and adjust the process properly [9, 5, 10, 11]. However, the documentation of the thermal history during AM processes poses significant challenges in terms of its feasibility and evaluation of the results [10]. Thermocouple measurements near the fusion line are well known to enable the determination of important information during LBW processes [12, 13]. In multi-layer deposition, the distance between the deposition point and the thermocouples in the substrate increases with increasing number of layers. Furthermore, the conduction conditions, especially in the early stages of the process, are strongly influenced by the presence of the substrate and might change with increasing structural height [14]. Thus,  
30 obtaining meaningful information by means of thermocouple measurements, es-

pecially for later stages of the deposition process, is difficult [15, 16, 17]. In this regard, thermography in terms of infrared (IR) camera observations is found to reveal important information regarding the temperature distribution along the whole deposition process [10, 16, 17, 18]. However, the quality of the results obtained strongly depends on the quality of calibration of the camera equipment, which necessitates a detailed analysis of possible measurement uncertainties, especially for the application during a dynamic process such as LMD [5, 18, 19]. A detailed investigation of the temperature evolution during the LMD process by a systematic variation of the laser irradiance is performed in this work. To  
40 achieve reliable results, the IR camera equipment is precisely tuned and an estimation of measurement errors is included in the analysis. Thus, a process monitoring is sought, which also allows conclusions about the process stability or changes of relevant temperature phenomena such as heat accumulation that directly affect the solidification process or residual stress distribution.

## 2. Laser Metal Deposition Process

A schematic view of the deposition process is shown in Fig. 1 (a). A three-axis, CNC-assisted machine centre was used for the deposition process, where local argon shielding gas of 10 l/min was applied onto the material through a nozzle. An Ytterbium fibre laser used for power supply was equipped on  
50 the  $z$  axis of the system working with a wavelength of 1070 nm. During the deposition, the Al-Mg wire (EN AW 5087) with a diameter of 1 mm was fed with a constant velocity onto the clamped substrate material (EN AW 5754; thickness of 3 mm) using an inclination angle of  $35^\circ$  in dragging configuration. In this regard, a unidirectional deposition strategy was chosen that has been reported to reduce heat accumulation within the deposited wall-like structure as compared to conducting bidirectional multi-layer deposition [17]. Moreover, in order to realize a relative high heat conduction into the underlying structure, a constant interlayer waiting time of approximately 60 s was used.

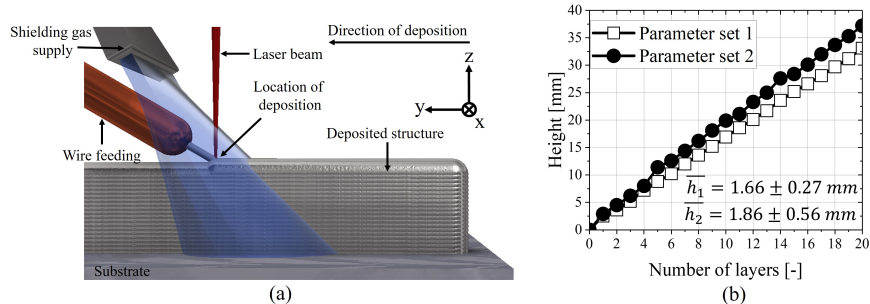


Figure 1: Schematic drawing of the deposition process for wire-based LMD (a) as well as the incremental height increase during deposition using the two investigated parameter sets (b).

It has previously been reported that this strategy has beneficial effects in terms of the development of a refined microstructure even for AM with high throughput of metallic material [20]. Energetic parameters such as the heat input or the specific energy input in order to achieve macroscopic defect-free structures have already been identified [2, 21]. As the laser irradiation  $I$  is one of the most significant parameters in laser fusion-based processes, this study is focused on its effect on the process stability and resulting temperature evolution. In this regard, two parameter sets, representing the minimum and maximum extreme case for the energy input but still producing defective-free structures are investigated. The minimum and maximum laser irradiation thresholds,  $1.10 \text{ kJ/mm}^2$  and  $2.20 \text{ kJ/mm}^2$ , are calculated according to the considerations of Leong and Geyer [7, 8]. In the following, parameter set 1 represents the maximum irradiation intensity, at which the process changes from conduction to deep penetration welding. Set 2 denotes the minimum irradiation intensity threshold, below which the process becomes unstable as not enough heat is provided. The investigated process boundaries therefore define the stable range of the process in which energetic adjustments are possible. The variation of the irradiation intensity was performed by a systematic adjustment of the focal position, while the laser power was kept constant. A summary of the process parameters applied is given in Table 1. 20 layers with a length of 280 mm using both sets

were deposited in order to achieve wall-like structures. Total structure heights  
of 33 mm and 37 mm by an average layer height of  $\bar{h}_1 = 1.66 \pm 0.27 \text{ mm}$  and  
 $\bar{h}_2 = 1.86 \pm 0.56 \text{ mm}$  for set 1 and 2 were achieved as illustrated in Fig. 1 (b).

Table 1: Summary of parameter sets representing the lower (set 2) and upper (set 1) irradiation thresholds.

Parameter	Symbol	Set 1	Set 2	Unit
Laser power	$P$	4000		W
Wire-feeding rate	$v_w$	10		m/min
Deposition velocity	$v_t$	1		m/min
Line energy	$E$	240		J/mm
Specific energy	$W_g$	11.5		kJ/g
Laser irradiance	$I$	2.20	1.10	kJ/mm <sup>2</sup>
Focal spot area	$A$	2.00	3.63	mm <sup>2</sup>

### 3. Characterization Methods

#### 3.1. Thermocouple Measurements

The substrate sheets were equipped with thermocouples from the backside as schematically shown in Fig. 2. The thermocouples were coated with a conductive paste and located 0.5 mm relative to the substrate surface after a distance of 140 mm from the start point of deposition.

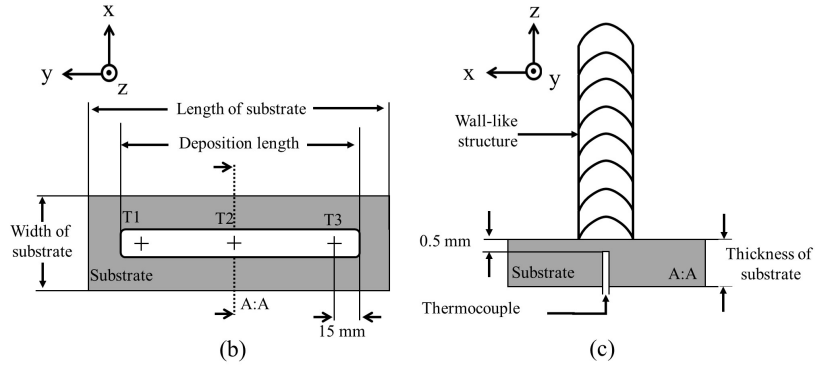


Figure 2: Schematic drawing of the substrate material and thermocouple positions inserted from the backside (a) as well as the identification of the thermocouple positions with respect to the substrate surface (b).

### 3.2. Thermography

Furthermore, an IR camera *Optris PI400* was focused to the centre of the specimens to be deposited having a vertical distance of 30 mm and horizontal distance of 200 mm, see Fig. 3. A safety distance, large enough to protect the optical lens of the camera from possible spatter and elevated temperatures but close enough to achieve reliable resulting in a spatial resolution of 0.68 mm/pixel, was chosen.

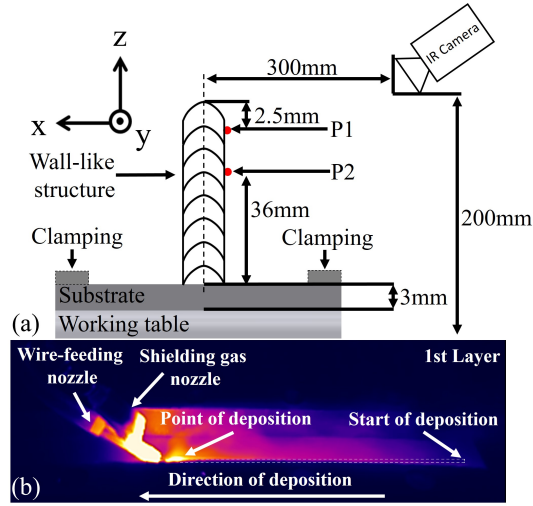


Figure 3: Schematic visualization of the IR thermography setup used in the experiments (a) together with an IR camera snapshot during the deposition of one exemplary layer (b).

The basic equation for calculating the temperature by measuring the emissivity of a material according to Stefan-Boltzmann law for non-black body on an normalized area is given as

$$E_T = \epsilon_\theta \sigma_\tau T^4 \quad (1)$$

where  $E_T$  is the specific radiance of the sample,  $\sigma_\tau$  is the Stefan-Boltzmann  
 90 constant and  $T$  represents the (thermodynamic) temperature of the sample  
 [10, 18, 22, 23]. The specific radiance is strongly dependent on the temperature-  
 dependent emission coefficient  $\epsilon_\theta$ , which therefore has to be calibrated precisely.  
 Two different temperature ranges were used for the measurements to obtain the

most accurate results in low ( $0 - 250^{\circ}\text{C}$ ) and high ( $150 - 950^{\circ}\text{C}$ ) temperature areas of the structures. Table 2 summarizes the most important data of the IR camera system according to the suppliers specifications used in the current study.

Table 2: Data of the IR camera system employed in the experimental study.

Parameter	Value	Unit
<b>Object lens</b>	$38 \times 29$	$^{\circ}$
<b>Spectral range</b>	$7.5 - 13$	$\mu\text{m}$
<b>1st working range</b>	$0 - 250$	$^{\circ}\text{C}$
<b>2nd working range</b>	$150 - 950$	$^{\circ}\text{C}$
<b>Resolution</b>	$382 \times 288$	pixel
<b>Frequency</b>	27 or 80	Hz

The emissivity of a material is strongly dependent on many parameters such as surface quality or the temperature itself [10]. Therefore, thermocouple measurements are used to calibrate the specific coefficient of emissivity  $\epsilon_{\theta}$ . Generally, the coefficient varies in a range between zero and one. In this regard,  $\epsilon_{\theta} = 1.0$  represents the theoretical ideal emission of a black body. However, the surface of the deposited structures shows a bright surface as the the smoke generated during the process settles on the structure produced. Consequently,  $\epsilon_{\theta}$  is expected to show a comparably low value. To account for this, two reference locations  $P1$  and  $P2$  were defined, as shown in Fig. 3, at which two thermocouples are fixed for the calibration of  $\epsilon_{\theta}$  within a preliminary study. The coefficient of emissivity was adjusted to yield equivalent temperature results at the reference positions for both thermocouples as well as thermographic measurements<sup>1</sup>. As reported by Yang et al. [10] and Frappier et al. [19], an assessment of uncertainty has to be conducted in order to check, whether IR measurements are relevant for precise temperature assessments.

<sup>1</sup>Due to the different distances to the deposition and therefore anticipated resulting temperatures, the IR camera is applied at  $P1$  using a working temperature range between  $150-950^{\circ}\text{C}$ , where the working temperature range  $0 - 150^{\circ}\text{C}$  is used at  $P2$ .

This calculation was performed using the considerations of Frappier et al [19], in which three basic contributions are stated to be considered in the total error  $|\Delta T|$  as

$$|\Delta T| = \sqrt{\Delta T_{\epsilon_{\theta}}^2 + \Delta T_{trans}^2 + \Delta T_{exp}^2}. \quad (2)$$

In this regard,  $\Delta T_{\epsilon_{\theta}}$  represents the error due to the uncertainty of  $\epsilon_{\theta}$  during the measuring process,  $\Delta T_{trans}$  the resulting error coming from the transformation of the IR intensity into direct temperature values and  $\Delta T_{exp}$  the experimental error caused by imprecise calibration and adjustment of the equipment. However, as Frappier et al. [19] discussed, in case of an application according to the producers specifications,  $\Delta T_{trans}$  and  $\Delta T_{exp}$  are certified to be neglectable. Therefore, solely  $\Delta T_{\epsilon_{\theta}}$  has to be taken into account and is determined as

$$|\overline{\Delta T}_{\epsilon_{\theta}}| = \frac{1}{n} \sum_{i=1}^n \sqrt{\left(\frac{T_{C_i} - T_{IR_i}(\epsilon_{\theta})}{T_{C_i}}\right)^2}. \quad (3)$$

$T_{C_i}$  is the temperature measured by thermocouple and  $T_{IR_i}(\epsilon_{\theta})$  the temperature measured by thermography for a specific coefficient of emissivity, at a specific location  $i$ . A relative error of  $|\overline{\Delta T}_{\epsilon_{\theta}}| = 2.81\%$  in case of  $P1$  as well as  $1.75\%$  in case of  $P2$  using  $\epsilon_{\theta} = 0.32$  was determined as shown in Fig. 4.

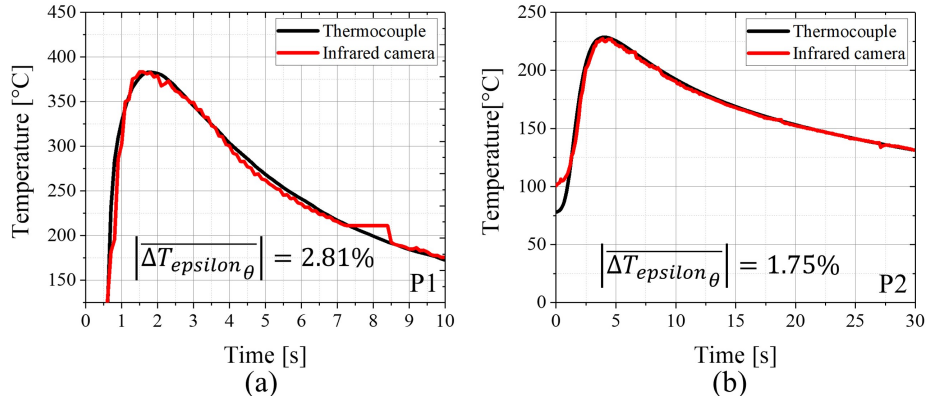


Figure 4: Comparison of temperature measurements via thermocouples and IR camera at position  $P1$  (a) and position  $P2$  (b) using  $\epsilon_{\theta} = 0.32$ . Good agreement between both measurement techniques is obtained.

### 3.3. Optical Microscopy

Representative cross and longitudinal sections were cut from the middle section of the samples. The samples were mounted, ground, polished and electrochemically etched using the Barker method to visualize the microstructural features of the Mg-containing Al alloy using polarized light through inverted optical microscopy (OM) Leica DMI 5000M. Using these metallographic inspections, information regarding the effect of different temperature evolutions on the microstructure are revealed.

## 4. Results and Discussion

### 4.1. Macroscopic Appearance

Multi-layer single-pass deposition of metals at high deposition rates is usually associated with poor surface qualities of the deposited structures [2]. This can partially be traced back to the fact that inhomogeneous solidification along the height of a deposited layer occurs. Particularly in case of high throughput deposition, the lower portion of the layer in the immediate vicinity of the previous layer solidifies faster than the remaining upper portion of the layer. In case of high throughput deposition, the required high energy inputs promote the development of high temperatures, strongly affecting the viscosity and surface tension of the liquid [24]. Furthermore, high feeding rates of the wire material additionally support the development of increased melt pool dynamics [5, 25]. As a result, the solidification is strongly affected and a more narrow layer thickness along the transition from the previous to the freshly deposited layers occurs, whereas more wide and flat layer geometries for the middle fraction of the layers develop [16]. This effect was recently investigated to be controllable by a systematic adjustment of the process parameters to some extent, thus enabling the tailoring of the geometrical shape of the layers [3].

Fig. 5 shows representative photographs of the surface quality of the deposited samples. The effective thickness of a deposited structure is determined by the deepest groove of the sample from both sides. Therefore, achieving a smooth surface of the deposited structure is important to maximize the effective thickness of the part and to minimize the amount of material to be removed. In this context, post processing such as milling is usually performed to achieve a high surface quality [2, 26, 27]. The surface of the structure processed with higher laser irradiance shows a few but large grooves, whereas parameter set 2, working with lower irradiance resulted in many fine surface grooves. The effective thickness after milling the deposited structures was measured to be  $t_{eff1} = 3.2\text{ mm}$  and  $t_{eff2} = 4.5\text{ mm}$ , which resulted in a thickness reduction of 33% in case of parameter set 1 and only 13% for parameter set 2. High thermal stresses, as expressed by large thermal expansions and contractions are assumed to increase the surface roughness by inhomogeneous material shrinkage during solidification [28]. In this context, the surface quality of a deposited sample can already provide first insights about the temperature development and homogeneity during the process.

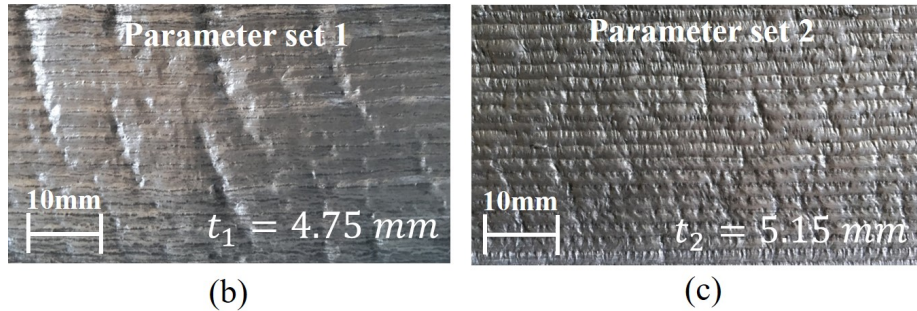


Figure 5: Optical photographs of the macroscopic surface appearance after wire-brush cleaning, taken from the middle of the wall structure for parameter set 1 (a) showing deep grooves and parameter set 2 (b), in which increased surface smoothness is observed.

The temperature evolutions measured in the middle of the deposition tracks via thermocouples, are plotted in Fig. 6 for the first five deposited layers. The two thermal histories reveal distinct differences between both parameter sets, especially regarding the peak temperatures. In case of parameter set 1, a peak temperature of  $\approx 470^\circ\text{C}$  during the deposition of the first layer is identified where this temperature is around  $110^\circ\text{C}$  lower in case of parameter set 2. This effect, related to the significantly reduced laser irradiance, already indicates significantly lower temperatures during multilayer deposition using parameter set 2. During the deposition of subsequent layers, the measured peak temperatures decrease due to the increased distance of the deposited material to the thermocouples in the substrate.

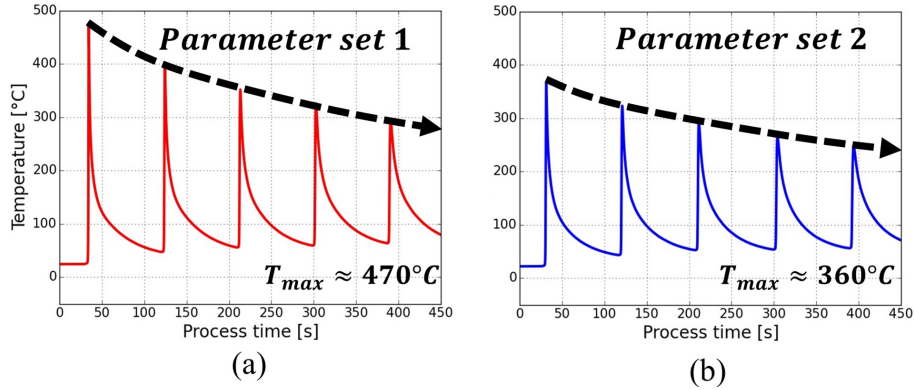


Figure 6: Thermal histories of the deposition process using parameter set 1 (a) and parameter set 2 (b) for the first five layers showing different peak temperatures between both sets as well as a general drop of measured temperature in the substrate due to the increasing distance between thermocouple tip and location of deposition.

In the following, results of IR thermography along the deposition up to the last  $20^{\text{th}}$  layer, plotted in 5-layer increments are provided, see Fig. 7. It can be seen that the structure processed by set 1 suffers higher thermal loads compared to set 2 as already observed from the thermocouple measurements. The increased laser irradiation in case of parameter set 1, results in heat accumulation within the Al structure.

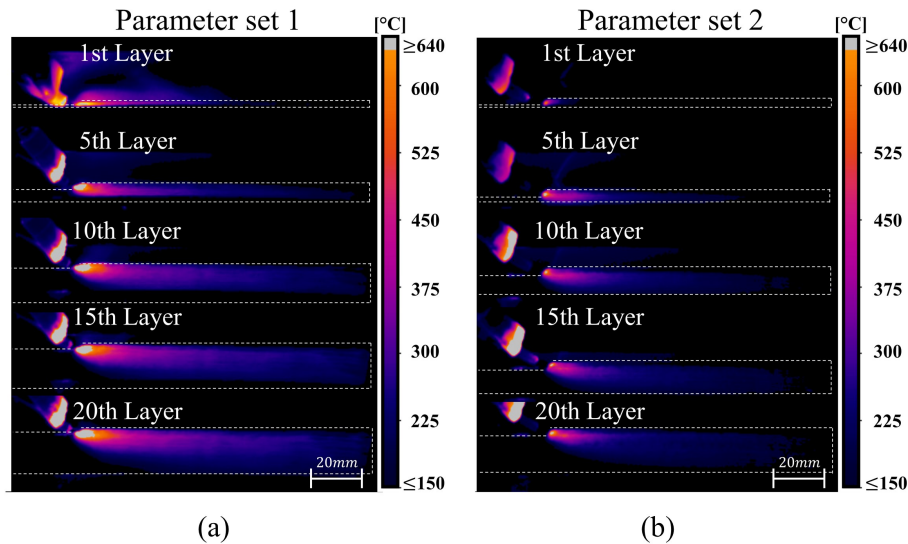


Figure 7: Temperature evolution of the deposition processes using IR thermography. An increasing heat accumulation along the deposition process can be seen in case of set 1 (a) whereas a stable temperature profile for set 2 (b) developed.

This is predominantly traced back to the fact that the introduced heat is not transferred completely along the Al structure and the substrate before a subsequent layer is deposited. This is supported by the fact, that the thermal conductivity of Al decreases for elevated temperatures above the melting point [24, 29, 30]. This supports the observation, that the thermal penetration into the subjacent structure increases with increasing number of layers. The remelting depth during early stages of the process was measured to be around 2 mm, which corresponds to a complete remelting of one previously deposited layer as well as fractions of the second last layer. During the deposition of the last layer, the remelting depth was determined to around 3 mm, which implies that around two layers are remelted during deposition. Despite its increase during the process, the observed remelting is comparatively low compared to WAAM of Al-Mg. Here remelting depths of up to 4 layers are reported by Oyama et al. [31], although the interlayer waiting time was twice as much. It can also be seen that a high volume of material is cyclically heated to high temperatures, which

is also associated with thermal expansion and contractions. Furthermore, this phenomenon aggravates with increasing number of layers.

In contrast, the temperature distribution observed for parameter set 2 shows less heat accumulations in the vicinity of the deposition location and along the structure. This indicates that the introduced heat is rapidly conducted along the structure before the deposition of a subsequent layer. During the full deposition process, the remelting depth during the deposition of subsequent layers were measured to be constantly less than one layer height. In summary, from these observations, it is concluded that a higher amount of energy is introduced into the material in the case of set 1, due to the higher irradiation intensity together with an increase of the absorption of Al in case of elevated temperatures [29, 30, 32]. This is supported by the increased temperature of the structure after the deposition of several layers. However, a more detailed analysis is needed for the comprehensive evaluation of the temperature distributions during the process.

In this regard, Fig. 8 (a) indicates the areas for temperature measurements presented in the following considerations. In Fig. 8 (b) the temperature difference measured in the middle of the structure, one second before and after the deposition of individual layers are plotted.

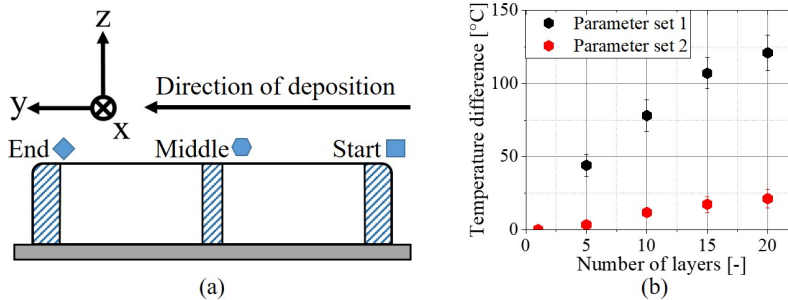


Figure 8: Identification of the measuring areas during the thermal comparison (a) as well as the temperature difference taken from the middle of the deposition tracks measured one second before the deposition of a respective layer and after completion (b).

An incremental heat accumulation during the process is seen for parameter set 1, whereas parameter set 2 results in a more constant and lower temperature difference. The influence of the substrate, which generates a strong heat conduction can be anticipated for both sets. The temperature difference doubles between the 5<sup>th</sup> and the 15<sup>th</sup> in case of set 1 from around 45°C to around 110°. By comparison, certain heat accumulation is also present for set 2 but significantly less pronounced. Approximately constant values after the deposition of the 5<sup>th</sup> layer are achieved. These observations indicate that in case of parameter set 2, stable deposition conditions are reached in early stages of the process. The comparison between the temperature before (a,b) and after (c,d) the deposition of respective layers taken from the start and end regions using the two parameter sets is plotted in Fig. 9.

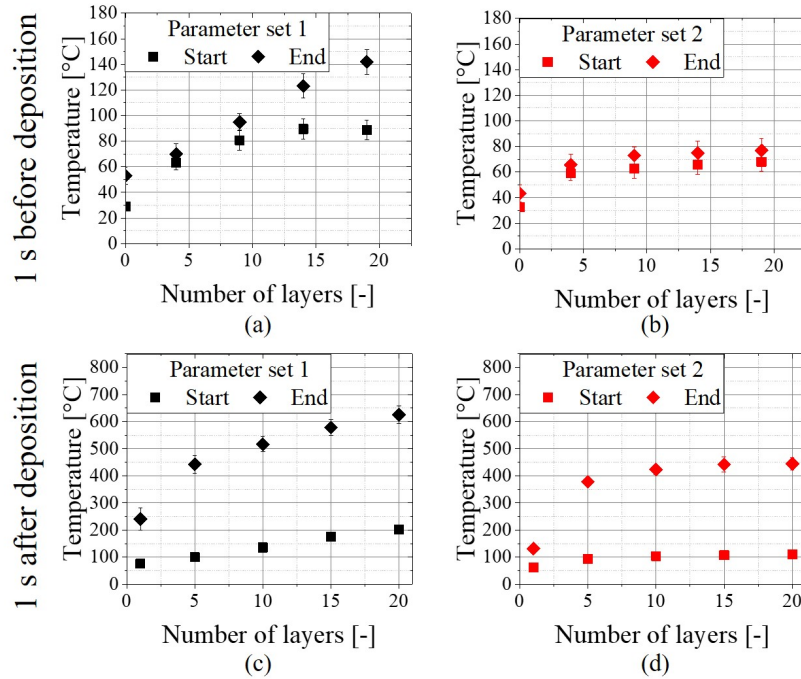


Figure 9: Comparison of the temperatures measured before the deposition of respective layers using set 1 (a) and 2 (b) as well as after (c,d) with respect to the difference between the start and ending regions of the tracks as indicated in Fig. 8.

The effect of the substrate vicinity regarding the heat conduction is still present but much less significant along the length of the layers. For set 1, it can be seen that both the global temperature of the structure as well as the temperature difference between the start and end of the deposited layers increase during the deposition process. The temperature at the beginning of the deposition tracks before the deposition, develops an almost constant value of  $\approx 80^\circ\text{C}$  after the completion of the 5<sup>th</sup> layer. By contrast, an approximate constant increase of the temperature of the end of the deposition tracks up to  $\approx 140^\circ\text{C}$  after the deposition of the 20<sup>th</sup> layer is evident. From this, the development of increasing thermal gradients along the longitudinal direction of the structure is deduced. This is not observable for set 2, in which an approximately constant temperature as well as temperature difference between start and end of the tracks is determined approximately after the deposition of the 5<sup>th</sup> layer (d). The temperature difference between the start and end regions in case of set 2 shows a constant value of  $\approx 60^\circ\text{C}$  already after the 5<sup>th</sup> layer. This behaviour is also observed after the deposition of layers.

The cooling rates within the 1<sup>st</sup>, 10<sup>th</sup> and 20<sup>th</sup> layer taken at a deposition length of 140 mm and averaged along time intervals of 0.5 s are shown in Fig. 10. In case of set 1 a maximum rate around  $200^\circ\text{C/s}$  for the first layer deposition is measured.

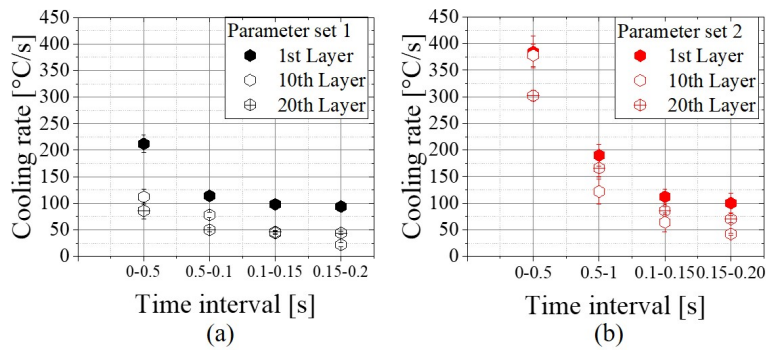


Figure 10: Exemplary cooling rates for parameter set 1 (a) and parameter set 2 (b) showing significantly increased cooling rates for set 2.

After the first defined time interval, the cooling rates show constant values with increasing time and increasing number of layers. This is in agreement with the analysis of the temperature evolution that indicated heat accumulation within the structure processed.

By contrast, the cooling rates for set 2 are much higher and differently characterized, see Fig 10 (b). A general decreasing slope along the analysed time intervals is evident, having the maximum rate during the first layer deposition around 400°C/s. The cooling rates along the 10<sup>th</sup> and 20<sup>th</sup> layer show a general decreasing slope with increasing time interval as well as approximately equal values between each other. This correspondence is an additional indication that the deposition process becomes constant with respect to the heat dissipation occurring during the process along the structure, as already assumed in the investigations of the temperature evolution. Significant differences in thermal stress and grain growth between the two sets of parameters can already be deduced from these results.

It is noted that the effective cooling rates directly during the solidification process are critical to the evolving stresses and microstructure. These are known to be many times higher than the cooling rates measured here after solidification of the material [2, 12]. However, the cooling rates at the time of solidification can not be measured with IR, since the melt emission would have to be known, which changes abruptly during solidification. In addition, during the transition from liquid to solid, the cooling rates would have been to be analysed for a time interval which is assumed to be multiple times less than the 0.5 s step size chosen here. The results shown, however, can be used for a qualitative comparison.

### 4.3. Temperature Gradients

The thermal contour plots during the deposition of the 20<sup>th</sup> layer are given in Fig. 11 for both parameter sets. The solidification conditions during AM of metals are strongly related to the temperature gradient  $G$ , given as

$$G = |\nabla T| = \sqrt{\left(\frac{\partial T}{\partial x}\right)^2 + \left(\frac{\partial T}{\partial y}\right)^2 + \left(\frac{\partial T}{\partial z}\right)^2} \quad (4)$$

and the solidification velocity  $R$  at any location along the solidification interface as

$$R = v_t \cos \theta \quad (5)$$

in which  $v_t$  is the travel speed of the heat source and  $\theta$  equals the angle between the main heat flow direction and the scanning direction of the heat source [2, 10, 33, 34]. It is well known that the relation between  $G$  and  $R$  reveals important information regarding the development of thermal stresses as well as grain growth behaviour [2, 5, 11, 12, 17]. In this regard, the development of high values of  $G$  supports the development of residual stresses in terms of the temperature gradient mechanism [35]. Regarding the microstructure, the ratio  $G/R$  determines the mode of solidification i.e. the grain morphology, and the product  $G \times R$  the size of the grains [2, 33]. The maximum growth rate appears in the centre of the melt pool in which the angle between the scanning direction and solidification direction is zero, i.e.  $R = v_t$  [2, 34].

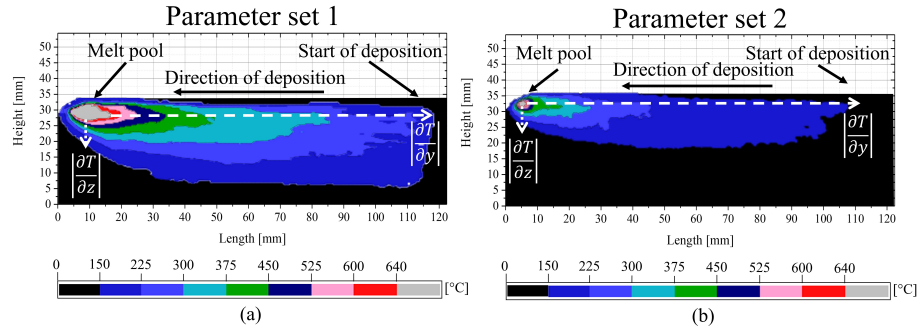


Figure 11: Thermal contour plots for the deposition of the 20<sup>th</sup> layer for set 1 (a) and 2 (b).

280 From the results shown in Fig. 11, representative calculations of the occurred thermal gradients, along the deposition track (dashed arrow)  $|\frac{\partial T}{\partial y}|$ , as well as in transverse direction (dotted arrow)  $|\frac{\partial T}{\partial z}|$  were performed. Due to the small thickness of the deposited structures, the gradients along the width are assumed to be neglectable as commonly done in AM of wall-like structures [2]. As expected, the process using parameter set 1 results in both an increased melt pool and heat affected zone (HAZ) compared to set 2.<sup>2</sup> The HAZ, in which thermal expansions and contractions occurred, was also significantly lower for set 2. The melting pool, depicted by temperatures above 640°C, is considerable larger in case of parameter set 1. A melt pool length of approximately 13 mm and 3  
290 mm along the deposition direction was determined for parameter set 1 and 2, respectively.

Temperature gradients obtained along the indicated arrows in Fig. 11 are plotted in Fig. 12. In case of parameter set 1, the thermal gradients along the longitudinal direction were less than 20°C/mm. In contrast, they exhibited an approximately linearly decreasing slope along the defined thermal contours regarding the transverse direction. The maximum thermal gradients showed values of  $|\frac{\partial T}{\partial y}| = 18^\circ\text{C}/\text{mm}$  and  $|\frac{\partial T}{\partial z}| = 102^\circ\text{C}/\text{mm}$ . From this it can be stated, that the gradient along the y-direction can also be neglected in case of set 1.

For parameter set 2, the thermal gradients along the transverse as well as the  
300 longitudinal direction show high similarities. Significantly higher gradients with nearly biaxial equal magnitudes were observed. The maximum values were measured to be  $|\frac{\partial T}{\partial y}| = 154^\circ\text{C}/\text{mm}$  and  $|\frac{\partial T}{\partial z}| = 172^\circ\text{C}/\text{mm}$ . By this, their difference is around 4 times lower than in case of set 1 and  $|\frac{\partial T}{\partial y}|$  has to be taken into account.

---

<sup>2</sup>It is noted that both the melt pool size and thermal gradients along the structures change during the deposition of an individual layer as well as for each subsequent layer.

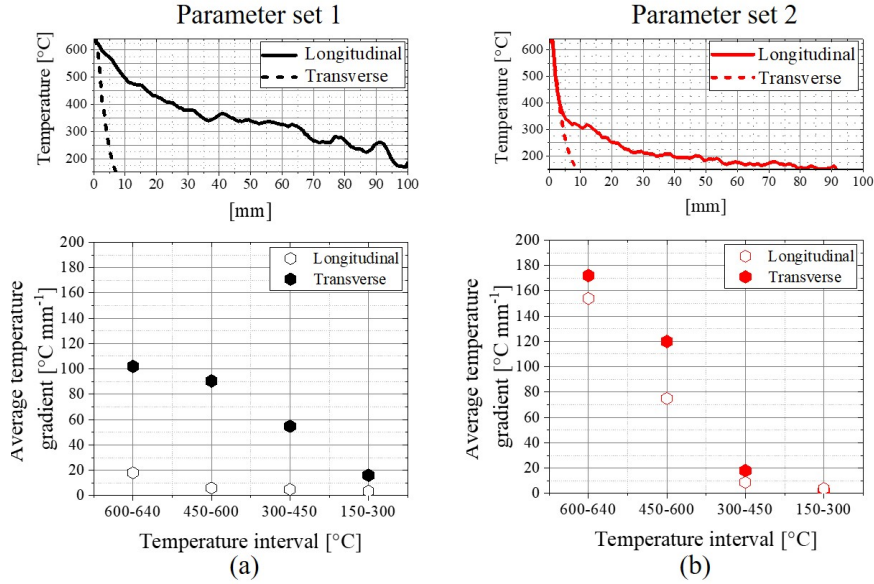


Figure 12: Thermal gradients during the deposition of the 20<sup>th</sup> layer using parameter set 1 (a) and parameter set 2 (b) in longitudinal and transverse direction, taken along the indicated arrows in Fig. 11 and measured by IR camera.

The thermal gradients analysed show distinct differences between the both sets. Thus, the resulting microstructure is also assumed to be considerably different. Therefore, a brief microstructural analysis is performed and discussed in the following with respect to the developing grain size and shape within the solidification structures.

310 *4.4. Microstructural analysis*

In Fig. 13 representative extractions along the height of the deposited structures at a deposition length of 140 mm are shown. Fig. 13 (a) and (b) illustrate cross and longitudinal sections from the structure processed with parameter set 1, where (c) and (d) show the corresponding microstructures from parameter set 2. Distinct differences in grain size and orientation are evident as expected by the consideration of the analysis of the temperature evolution and thermal gradients during the processes.

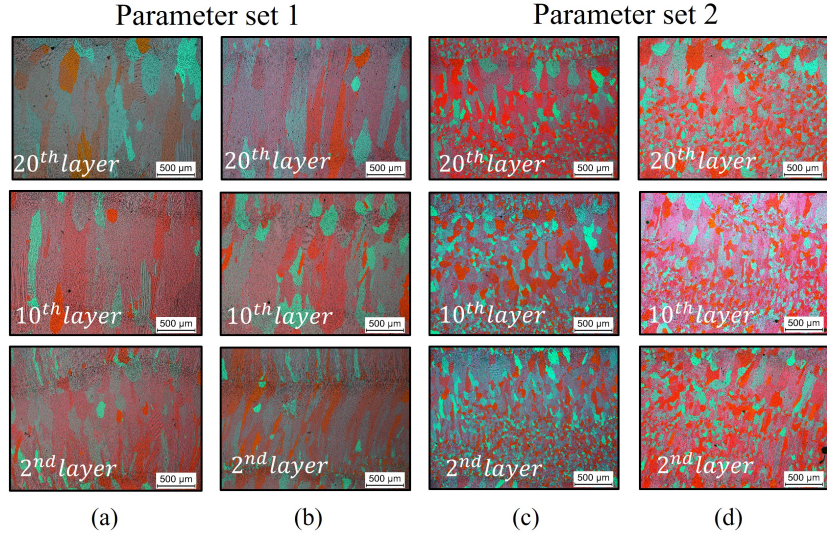


Figure 13: Cross (a,c) and longitudinal (b,d) sections taken at a deposition length of 140 mm showing large columnar grains along the sample in case of set 1 (a,b) as well as a refined microstructure and more equiaxed grain growth in case of set 2 (c,d).

As expected, the corresponding microstructure processed by set 1, shows a typical columnar solidification structure along the height of the sample. In contrast, a lower laser irradiance (set 2) leads to a refined microstructure including coarser and finer grained areas along the height. In this regard, the determined average grain sizes  $d_{av}$  according to DIN ISO 643 standard [36] are shown in Fig. 14. It can be seen that the grain sizes in the early stages of the process are significantly smaller than at later phases for both parameter sets, which is agreement with the observation of increased cooling rates and penetration depths in early stages of the processes for both sets. With parameter set 1, the grain size increases for the entire process along the height. The slope of the grain size, decreasing for increasing number of layers, shows similarities to the observations of increasing heat accumulation and decreasing cooling rates during the deposition process for set 1. Therefore, it is assumed that the temperature gradients also decrease for increasing number of layers. Thus, coarsening and inhomogeneity of the microstructure develops along the height of the structure.

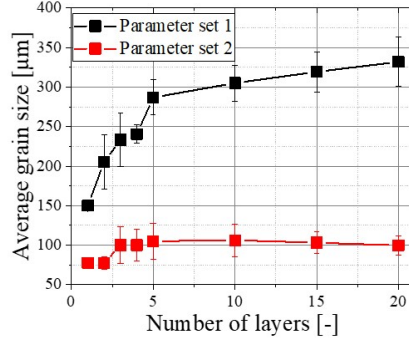


Figure 14: Average grain size along the height of the structures, measured according to DIN ISO 643 [36]. Distinct differences between the parameter sets as well as with increasing distance to the substrate are shown.

The observations during the thermal analysis are also reflected by the resulting solidification microstructure for parameter set 2. An increase in the average grain size can be seen only for the first layers, in which also higher cooling rates were measured. The rest of the structure shows almost constant average grain sizes along the height. This consistency was also observed for the developing process temperature during the deposition process for set 2. The determined products of  $G$  and  $R$  during the deposition of the 20<sup>th</sup> layer yield in values of 1700°C/s and 5433°C/s for set 1 and 2. This is a difference by around factor 3.2, which is approximately equal to the difference of the average grain sizes between the two structures processed. It has to be noted, that the determination of  $G$  is strongly dependent on the isothermal range, in this case 600 – 640°C. For this reason, the current gradients are calculated with a maximum value of 640°C. However, the actual gradient between the melt and the solidification line is assumed to be much higher as melt pool temperatures in a range of  $10^3$  °C typically develop [31, 37]. Therefore, the effective temperature gradient  $G$  is an underestimation, but as already stated for the cooling rates, it is applicable for a qualitative comparison. The dominant temperature gradient  $|\frac{\partial T}{\partial z}|$  in case of parameter set 1 supported an elongated grain morphology along the building direction.

By contrast, the development of approximate biaxial thermal gradients in  $y$  and  $z$  direction resulted in more equiaxed grain morphologies in case of set 2. The aspect ratio was calculated as a relation between the minor to the major axis of the grains  $d_{min}/d_{maj}$  within the 20<sup>th</sup> layer. A summary of the calculated solidification characteristics using Eqs. (4) and (5) as well as analysed microstructural features is given in Table 3.

Table 3: Result summary of calculated values for  $G$  and  $R$  during the deposition of the 20<sup>th</sup> layer as well as characteristic features of the solidification microstructures regarding average grain sizes and morphologies.

Parameter	Symbol	Set 1	Set 2	Unit
Solidification rate	$R$	16.67		mm/s
Temperature gradient	$G$	102	326	°C/mm
Solidification mode	$G/R$	6.1	19.6	°C·s/mm <sup>2</sup>
Solidification scale	$G \times R$	1700	5433	°C/s
Average grain size	$d_{av}$	332	99	$\mu\text{m}$
Grain aspect ratio	$d_{asp}$	0.36	0.82	-

## 5. Conclusions

This contribution presents a detailed characterization of the thermal profile in wire-based LMD of multilayer Al-Mg structures using a systematic laser irradiation adaptation. Minimum and maximum possible laser irradiation intensities were used, representing the extreme cases within the possible process parameter window. The structures showed significantly different surface qualities as well as microstructural features. IR thermography turned out to be a powerful tool to assess the wire-based LMD processes of Al-Mg in terms of process stability, heat dissipation phenomena and developing solidification microstructure. Based on the experimental results presented and discussed in this paper, the following conclusions are drawn:

- Distinct differences can be achieved by a systematic variation of the laser irradiation while keeping process energies such as line and specific energy constant.

- The resulting solidification microstructure is strongly related to evolving temperature profiles, making a tailoring of microstructures possible by controlling the process temperature.
- The application of a maximum irradiation intensity results in a poor surface quality together with the development of a coarse microstructure, associated with strong heat accumulations within the structure and high fractions of remelting during the deposition process.
- Reduced irradiation intensities result in improved surface quality as well as a refined and constant microstructure that is produced as a result of increased cooling rates and high biaxial thermal gradients  $|\frac{\partial T}{\partial y}|$  and  $|\frac{\partial T}{\partial z}|$ .

380

### Acknowledgements

The authors would like to thank Mr. R. Dinse, Mr. P. Haack and Mr. F. Dorn from Helmholtz-Zentrum Geesthacht for their valuable technical support.

### References

- [1] Schmidt M, Merklein M, Bourell D, Dimitrov D, Hausotte T, Wegener K, et al. Laser based additive manufacturing in industry and academia. CIRP Annals - Manufacturing Technology 2017;doi:<http://dx.doi.org/10.1016/j.cirp.2017.05.011>.
- [2] DebRoy T, Wei H, Zuback J, Mukherjee T, Elmer J, Milewski J, et al. Additive manufacturing of metallic components process, structure and properties. Progress in Materials Science 2018;92:112 – 224. doi:<https://doi.org/10.1016/j.pmatsci.2017.10.001>.
- [3] Froend M, Riekehr S, Kashaev N, Klusemann B, Enz J. Process development for wire-based laser metal deposition of 5087 aluminium alloy by using fibre laser. Journal of Manufacturing Processes 2018;34:721 –32. doi:<https://doi.org/10.1016/j.jmapro.2018.06.033>.

390

- 400 [4] Shamsaei N, Yadollahi A, Bian L, Thompson SM. An overview of direct laser deposition for additive manufacturing; part ii: Mechanical behavior, process parameter optimization and control. *Additive Manufacturing* 2015;8:12 – 35. doi:<https://doi.org/10.1016/j.addma.2015.07.002>.
- [5] Thompson SM, Bian L, Shamsaei N, Yadollahi A. An overview of direct laser deposition for additive manufacturing; part i: Transport phenomena, modeling and diagnostics. *Additive Manufacturing* 2015;8:36 – 62. doi:<https://doi.org/10.1016/j.addma.2015.07.001>.
- [6] Demir AG, Biffi CA. Micro laser metal wire deposition of thin-walled alloy components: Process and material characterization. *Journal of Manufacturing Processes* 2019;37:362 –9. doi:<https://doi.org/10.1016/j.jmapro.2018.11.017>.
- 410 [7] Leong K, Geyer H. Threshold laser beam irradiances for melting and welding. *Journal of Laser Applications* 1997;9(5):227–31.
- [8] Leong K, Geyer H. Laser beam welding of any metal. *Proceedings of the International Congress on Applications of Laser and Electro-Optics (ICALEO)* 1998;:243–51.
- [9] Herrnring J, Staron P, Kashaev N, Klusemann B. Multiscale process simulation of residual stress fields of laser beam welded precipitation hardened AA6082. *Materialia* 2018;3:243 –55. doi:<https://doi.org/10.1016/j.mtla.2018.08.010>.
- 420 [10] Yang D, Wang G, Zhang G. Thermal analysis for single-pass multi-layer GMAW based additive manufacturing using infrared thermography. *Journal of Materials Processing Technology* 2017;244:215 –24. doi:<https://doi.org/10.1016/j.jmatprotec.2017.01.024>.
- [11] Baere DD, Bayat M, Mohanty S, Hattel J. Thermo-fluid-metallurgical modelling of the selective laser melting process chain. *Procedia CIRP* 2018;74:87 – 91. doi:<https://doi.org/10.1016/j.procir.2018.08.035>.

- [12] Hekmatjou H, Naffakh-Moosavy H. Hot cracking in pulsed Nd:YAG laser welding of AA5456. *Optics and Laser Technology* 2018;103:22 – 32. doi:<https://doi.org/10.1016/j.optlastec.2018.01.020>.
- [13] Zhou L, Luo L, Tan C, Li Z, Song X, Zhao H, et al. Effect of welding speed on microstructural evolution and mechanical properties of laser welded  
430 brazed Al/brass dissimilar joints. *Optics and Laser Technology* 2018;98:234 –46. doi:<https://doi.org/10.1016/j.optlastec.2017.08.004>.
- [14] Froend M, Ventzke V, Riekehr S, Kashaev N, Klusemann B, Enz J. Microstructure and microhardness of wire-based laser metal deposited AA5087 using an Ytterbium fibre laser. *Materials Characterization* 2018;143:59 – 67. doi:<https://doi.org/10.1016/j.matchar.2018.05.022>.
- [15] Froend M, Bock F, Riekehr S, Kashaev N, Klusemann B, Enz J. Experimental investigation of temperature distribution during wire-based laser metal deposition of the al-mg alloy 5087. vol. 941 MSF. Trans Tech Publications Ltd. ISBN 9783035712087; 2018, p. 988–94. doi:10.4028/www.  
440 [scientific.net/MSF.941.988](https://www.scientific.net/MSF.941.988).
- [16] Bock F, Froend M, Herrnring J, Enz J, Kashaev N, Klusemann B. Thermal analysis of laser additive manufacturing of aluminium alloys: Experiment and simulation. *AIP Conference Proceedings* 2018;1960. doi:<http://dx.doi.org/10.1063/1.5034996>.
- [17] Nikam SH, Jain NK. Three-dimensional thermal analysis of multi-layer metallic deposition by micro-plasma transferred arc process using finite element simulation. *Journal of Materials Processing Technology* 2017;249:264 –73. doi:<https://doi.org/10.1016/j.jmatprotec.2017.05.043>.
- [18] Vollmer M, Möllmann K. *Infrared Thermal Imaging: Fundamentals, Research and Applications*; vol. 2; chap. 1-3. Wiley-VCH. ISBN 9783527693320; 2017,.  
450

- [19] Frappier R, Benoit A, Paillard P, Baudin T, Le Gall R, Dupuy T. Quantitative infrared analysis of welding processes: Temperature measurement during rsw and cmt-mig welding. *Science and Technology of Welding and Joining* 2014;19(1):38–43. doi:<https://doi.org/10.1179/1362171813Y.0000000158>.
- [20] Gu J, Wang X, Bai J, Ding J, Williams S, Zhai Y, et al. Deformation microstructures and strengthening mechanisms for the wire+arc additively manufactured Al-Mg4.5Mn alloy with inter-layer rolling. *Materials Science and Engineering: A* 2018;712:292 – 301. doi:<https://doi.org/10.1016/j.msea.2017.11.113>.
- [21] Froend M, Ventzke V, Riekehr S, Kashaev N, Klusemann B, Enz J. Microstructure and hardness evolution of laser metal deposited AA5087 wall-structures. vol. 74. 2018, p. 131 –5. doi:<https://doi.org/10.1016/j.procir.2018.08.062>.
- [22] Herwig H, Moschallski A. *Wärmeübertragung:Physikalische Grundlagen*; vol. 3. Springer Vieweg. ISBN 978-3-658-06208-8; 2014, p. 21–61. doi:<https://doi.org/10.1007/978-3-658-06208-8>.
- [23] Bai X, Zhang H, Wang G. Improving prediction accuracy of thermal analysis for weld-based additive manufacturing by calibrating input parameters using ir imaging. *The International Journal of Advanced Manufacturing Technology* 2013;69(5):1087–95. doi:10.1007/s00170-013-5102-y.
- [24] Kammer C. *Aluminium-Taschenbuch*. 1. Grundlagen und Werkstoffe; vol. 16 of *Aluminium-Taschenbuch*. Beuth Praxis. ISBN 9783870172749; 2002,.
- [25] Arrizubieta JI, Lamikiz A, Klocke F, Martinez S, Arntz K, Ukar E. Evaluation of the relevance of melt pool dynamics in laser material deposition process modeling. *International Journal of Heat and Mass Transfer* 2017;115:80 – 91. doi:<https://doi.org/10.1016/j.ijheatmasstransfer.2017.07.011>.

- [26] Frazier WE. Metal Additive Manufacturing: A Review. *Journal of Materials Engineering and Performance* 2014;23(6):1917–28. doi:10.1007/s11665-014-0958-z.
- [27] Syed WUH, Pinkerton AJ, Li L. A comparative study of wire feeding and powder feeding in direct diode laser deposition for rapid prototyping. *Applied Surface Science* 2005;247(1):268–76. doi:http://dx.doi.org/10.1016/j.apsusc.2005.01.138.
- [28] Szost BA, Terzi S, Martina F, Boisselier D, Prytuliak A, Pirling T, et al. A comparative study of additive manufacturing techniques: Residual stress and microstructural analysis of CLAD and WAAM printed Ti6Al4V components. *Materials and Design* 2016;89:559–67. doi:http://dx.doi.org/10.1016/j.matdes.2015.09.115.
- 490 [29] Palik ED. Chapter 3 - Thermo-Optic Coefficients. Burlington: Academic Press. ISBN 978-0-12-544415-6; 1997, p. 115 – 261. doi:https://doi.org/10.1016/B978-012544415-6.50150-3.
- [30] Stern F. Absorptivity of cw CO<sub>2</sub>, CO and YAG-laser beams by different metallic alloys. *Proceedings of the 3rd European Conference of Laser Treatment of Materials (ECLAT)* 1990;3:25–35.
- 500 [31] Oyama K, Diplas S, M'hamdi M, Gunns AE, Azar AS. Heat source management in wire-arc additive manufacturing process for al-mg and al-si alloys. *Additive Manufacturing* 2019;26:180–92. doi:https://doi.org/10.1016/j.addma.2019.01.007.
- [32] Steen W, Mazumder J. *Basic Laser Optics*; vol. 4. 2010, p. 199–249. doi:https://doi:10.1007/978-1-84996-062-5-3.
- [33] Wei H, Mazumder J, Debroy T. Evolution of solidification texture during additive manufacturing. *Scientific Reports* 2015;5(16446). doi:10.1038/srep16446.

- 510 [34] Rosenthal D. The theory of moving sources of heat and its application to metal treatments; vol. 43. 1946, p. 849–66.
- [35] Froend M, Fomin F, Riekehr S, Alvarez P, Zubiri F, Bauer S, et al. "Fiber laser welding of dissimilar titanium (Ti-6Al-4V/cp-Ti) T-joints and their laser forming process for aircraft application". *Optics & Laser Technology* 2017;96:123 –31. doi:<https://doi.org/10.1016/j.optlastec.2017.05.017>.
- [36] International Organization for Standardization - Micrographic determination of the apparent grain size (ISO 643). 2013.
- [37] Mukherjee T, Zhang W, DebRoy T. An improved prediction of residual stresses and distortion in additive manufacturing. *Computational Materials Science* 2017;126:360 –72. doi:<https://doi.org/10.1016/j.commatsci.2016.10.003>.  
520